# Self-propelled magnetic microrobots for photodynamic cancer therapy

Xia Peng[1], Mario Urso[1], Jan Balvan[2,5], Michal Masarik[2,5,6], Martin Pumera[1,3,4*]

[1] Future Energy and Innovation Laboratory, Central European Institute of Technology, Brno University of Technology, Purkynova 123, 61200, Brno, Czech Republic

[2] Department of Physiology, Faculty of Medicine, Masaryk University, Kamenice 5, 62500 Brno, Czech Republic

[3] Department of Medical Research, China Medical University Hospital, China Medical University, No. 91 Hsueh-Shih Road, TW-40402 Taichung, Taiwan

[4] Department of Chemical and Biomolecular Engineering, Yonsei University, 50 Yonsei-ro, Seodaemun-gu, Seoul 03722, Korea

[5] Department of Pathological Physiology, Faculty of Medicine, Masaryk University/Kamenice 5, CZ-625 00, Brno, Czech Republic

[6]BIOCEV, First Faculty of Medicine, Charles University, Prumyslova 595, CZ-252 50 Vestec, Czech Republic

* Corresponding author e-mail: martin.pumera@ceitec.vutbr.cz

## Abstract

Photocatalytic microrobots that possess the advantageous features of wireless steering and controllable motion by light have been extensively explored as photodynamic therapy (PDT) for cancer treatment. However, overexpressed glutathione (GSH) in the tumor microenvironment can down-regulate the reactive oxygen species (ROS) level for cancer therapy. Herein, we present fin-shaped light-powered hematite microrobots as an effective GSH depletion agent for PDT of prostate cancer cells. These hematite microrobots, synthesized by a facile one-step method without any further surface functionalization, can exhibit negative photogravitactic motion under light irradiation and flexible actuation in a defined path controlled by an external rotating magnetic field. Non-contact transportation of micro-sized cells can also be achieved by manipulating the movement of a single microrobot, allowing remote control of micro-objects without contamination. In addition, the biocompatible microrobots induce GSH depletion and greatly enhance the PDT performance. The proposed low-cost single-component hematite microrobots contribute to developing noble metal-free dual light/magnetic field-powered micromachines for the biomedical field.

## Introduction

Inspired by the extensive photosynthesis process in nature, artificial microrobots that consist of "smart materials" with intrinsic capacity or functionalized integration can similarly convert light sources into energy for autonomous motion, which can be induced by different mechanisms, including self-electrophoresis, self-diffusiophoresis, and bubble propulsion.[1–3] These light-powered self-propelled microrobots have gained considerable interest over the past decades due to their remote and controllable motion by an external renewable and abundant light energy source, additionally, their great potential in various fields, i.e., sensing, imaging, drug delivery, and environmental remediation.[4–8] Plenty of photocatalytic materials ($TiO_2$, ZnO, $Fe_2O_3$, BiOI) have been exploited as the main constituent for the fabrication of innovative light-powered microrobots.[9–15] Breaking the material's symmetry by the uneven deposition of a noble metal coating represents a promising strategy to endow them with an effective motion by light irradiation. For instance, the $TiO_2$ microparticles with Au half-coating exhibited motion behavior once exposed to UV-light by self-electrophoresis, i.e., under the action of a local electric field induced by the asymmetrical generation of a charged products gradient.[2] In addition, light-powered fuel-free ZnO/Pt Janus micromotors are capable of aligning themselves to illumination direction and exhibiting negative phototaxis at high speeds.[16] However, the dependence on expensive noble metals remains a challenge in the micro/nanorobotics field, not only for light-powered but also for fuel-driven micro/nanorobots.[17, 18] On the other hand, magnetic nanoparticles are extensively integrated on the surface of light-powered microrobots in order to achieve precisely controllable motion for biomedical applications.[19, 20] As a consequence, simple, metal-free, inherently magnetic, and low-cost light-driven microrobots are highly desired for real-world applications.

Given the tremendous progress in nanotechnology and nanomaterials in the biomedical field, many therapeutic approaches have been developed for cancer treatments, such as chemotherapy, gene therapy, radiotherapy, immunotherapy, and PDT.[21] Among them, PDT has received extensive attention as an emergent and promising drug-free cancer treatment method. [22–24] PDT employs photocatalysts that can convert oxygen molecules into ROS, which can cause permanent damage to cancer cells.[25, 26] However, overexpression of GSH in tumor cells greatly inhibits the therapy effect of PDT. Reducing the level of GSH in tumor cells to improve the amount of ROS produced is very important to destroy the cellular antioxidation defense system, synergistically killing cancer cells.[27] The employment of photocatalytic materials to develop light-powered microrobots capable of active propulsion and producing ROS provides an emerging and promising tool to oxidize GSH and maximize the benefit of cancer treatment.

In this work, we propose metal-free fin-structured hematite microrobots with dual magnetic/optical propulsion mode for effective GSH depletion, increasing the cytotoxicity against prostate cancer cells. Fin-structured hematite microparticles were synthesized in one step by a simple and facile hydrothermal reaction. The metal-free hematite microrobots exhibit negative phototactic motion when exposed to light irradiation due to the relative planar and asymmetric fin-like structure. Thanks to the inherent magnetism of hematite, the microrobots can be precisely navigated following any arbitrary trajectory under a transversal rotating magnetic field. Taking advantage of these features, the non-contact transportation of targeted microscale objects, such as cells, can be achieved using hematite microrobots by generating a localized fluid flow. The prostate cancer cells were selected to examine the PDT capacity of hematite microrobots. Under exposure to light in the presence of $H_2O_2$, the hematite microrobots produce abundant ROS to induce GSH depletion and greatly enhance the PDT efficiency against prostate cancer cells. These results demonstrate that the fin-structured hematite microrobots can be a superior adjuvant for augmenting cancer therapeutic efficacy and holds great promise for future biomedical applications.

## Result and Discussion

**Figure 1** depicts the fabrication process and characterization of hematite microrobots. In order to obtain single-component hematite microrobots, a simple and low-cost hydrothermal reaction was employed, as schematically shown in **Figure 1A**. Scanning electron microscopy (SEM) images at different magnifications of hematite microrobots are shown in **Figure 1B**. The low-magnification SEM image reveals the hematite microrobots' uniform and symmetric fin-like structure (**Figure 1B**). The lengths of central trunks are approximately 8−10 μm. The high-resolution SEM image shows an attractive fractal structure, with a distinct trunk and highly organized branches distributed on both sides of the trunk. Furthermore, the sub-branches with an identical fin-like structure and relatively smaller size were growing on the main branches. This hierarchical and asymmetrical fin-like structure, which provides abundant catalytic active sites with considerable edges along with trunks, facilitates the migration of diverse chemical species beneficial for the motion of microrobots and their potential applications. Energy-dispersive X-ray spectroscopy (EDX) elemental mapping images validates the presence and uniform distributions of Fe and O elements, as displayed in **Figure 1B.** The X-ray diffraction (XRD) pattern of hematite microrobots is shown in **Figure 1C**, indicating that the synthesized microrobots can be well indexed to the standard hexagonal hematite phase (JCPDS no.

33−0664). The main diffraction peaks at 24.2°, 33.2°, 35.6°, 40.9°, 49.5°, and 54.1° are ascribed to (012), (104), (110), (113), (024), and (116) crystal facets, respectively.[28] The chemical composition of hematite microrobots was further examined by X-ray photoelectron spectroscopy (XPS). **Figures 1D and E** show the high-resolution XPS spectra of Fe 2*p* and O 1*s*, respectively. In the high-resolution Fe 2*p* spectrum (**Figure 1D**), two peaks at binding energies of ~711 eV for Fe $2p_{3/2}$ and ~724 eV for Fe $2p_{1/2}$ with the corresponding satellite peaks at ~719 and ~733 eV binding energies can be distinguished. These are characteristics of $Fe^{3+}$ ions in hematite.[29] The high-resolution O 1*s* spectrum shows two contributions at ~532 eV and ~530 eV binding energy, assigned to Fe-O within $Fe_2O_3$, and OH groups bonded to FeO within FeO(OH), respectively.

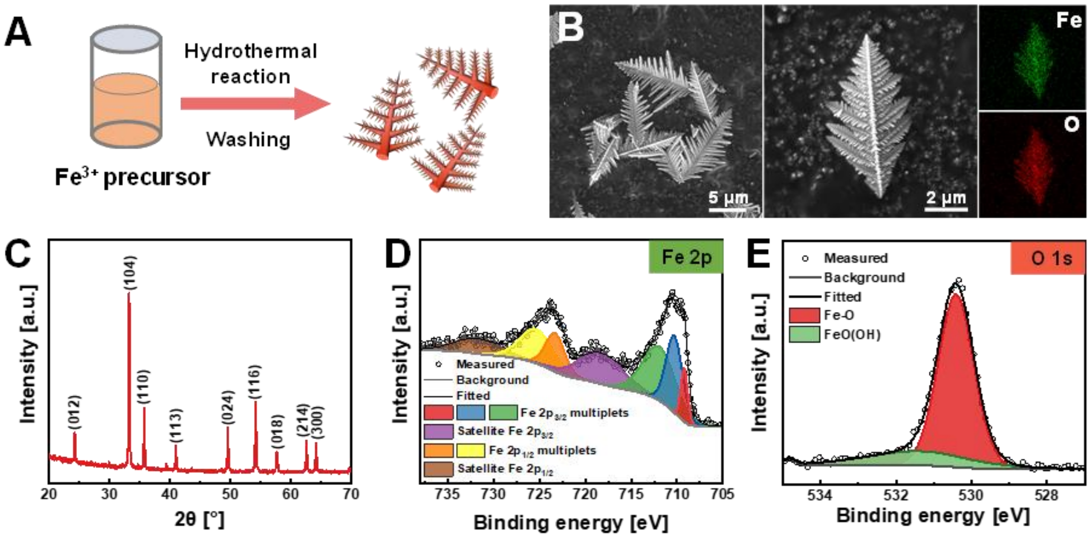

**Figure 1.** Synthesis and characterization of fin-shaped hematite microrobots. A) Schematic illustration of the synthetic procedure. B) SEM images at different magnifications and EDX mapping images. C) XRD pattern. D) Fe 2*p* XPS spectrum. E) O 1*s* XPS spectrum.

The motion behavior of hematite microrobots was evaluated in pure water under UV-light irradiation. The self-propulsion mechanism of single-component light-powered microrobots has been elucidated in previous works.[30–31] As demonstrated in **Figure 2A**, hematite absorbs light with energy equal to or higher than its bandgap to produce photogenerated electron-hole pairs in its valence (VB) and conduction bands (CB). The photogenerated electrons can react with oxygen in the media or $H_2O_2$ molecules to generate ROS, including •OH, and $•O^{2-}$, whereas the photogenerated holes are able to oxidize water into hydroxyl radicals or decompose $H_2O_2$ into oxygen and protons ($H^+$). The hierarchical structure of hematite microrobots and non-uniform light exposure (light source located underneath the glass slide) results in an asymmetrical photogeneration of chemical species that creates a localized electrolyte gradient around the microrobots, prompting their autonomous motion by self-electrophoresis. The optical bandgap ($E_g$) of hematite microrobots in **Figure 2B** was calculated from the UV-Vis absorption spectrum using the Tauc plot.[32] The estimated $E_g$ value is 2.02 eV, proving that the optical absorption of hematite microrobots lies in the visible region. To gain insight into the oxidizing properties of hematite microrobots under light, we measured the mixed potential values from Tafel plot curves of the hematite microrobots under dark and light irradiation in pure water. As shown in **Figure 2C**, the mixed potential value of hematite shifts to more negative potentials ($\Delta E_{\text{Dark: Light}} = 40$ mV), indicating that the hematite can oxidize $H_2O$ under light irradiation.[33] The speed of microrobots in pure water was merely $2.5 \pm 0.5$ μm $s^{-1}$, but it progressively increased to $18 \pm 5$ μm $s^{-1}$ when a higher concentration of $H_2O_2$ solution was introduced (**Figure 2D**). Photocatalytic decomposition of $H_2O_2$ at the downside surface of hematite microrobots proceeds according to the reaction scheme in **Equation (1)**[28]

$$\begin{aligned} &\alpha\text{-}Fe_2O_3 + h\nu \rightarrow e^- + h^+. \\ &H_2O_2 + 2h^+ \rightarrow 2H^+ + O_2. \\ &H_2O_2 + 2e^- + 2H^+ \rightarrow 2H_2O. \end{aligned} \tag{1}$$

As shown in **Figure 2E**, captured from **Supplementary Movie 1**, an enhanced wall-bound 2D motion of the microrobots rather than Brownian motion can be observed at a low $H_2O_2$ concentration under light irradiation. Interestingly, when the higher $H_2O_2$ concentration was employed, the microrobots displayed a "lift-off" transition. As shown in the time-lapse images in **Figure 2F**, the microrobots exhibit powerful propulsion and move upwards against gravity, away from the bottom wall. They immediately swim out of focus, showing a negative photogravitaxis (**Supplementary Movie 1**).[34-36] When the light is turned off, the microrobots gradually move back to the glass wall plane and get focused again. As schematically illustrated in **Figure 2G**, microrobots can decompose water and $H_2O_2$ into various chemical species on the side close to the glass wall when asymmetrical UV-light illumination is turned on. The chemical gradient on the downside surface of microrobots can overcome the constraint of the gravitational force, prompting light-controlled swimming activity in the three-dimensional (3D) space. When UV light is turned off, the generation of chemical species is hampered and gravity becomes the dominant driven force.

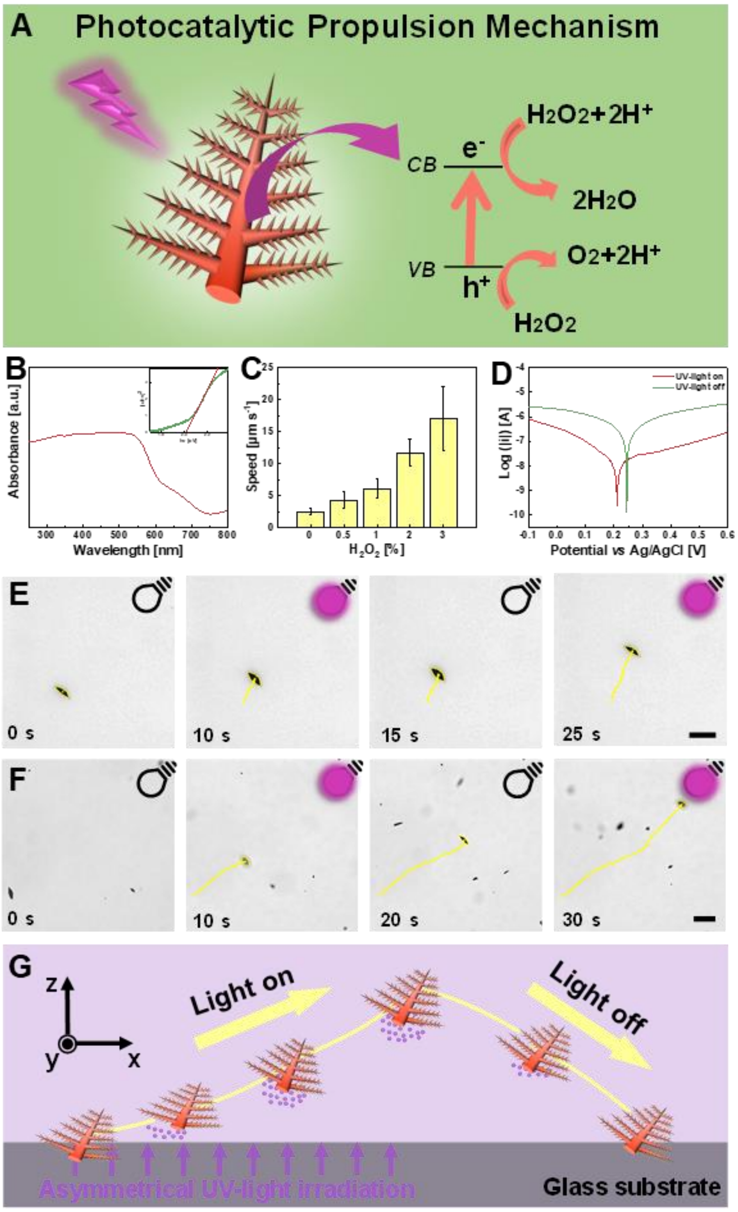

**Figure 2.** Motion behavior of hematite microrobots. A) Schematic illustration of the photocatalytic activation and their self-propulsion mechanism. B) UV−Vis absorbance spectrum of the hematite microrobots. The inset reports the corresponding Tauc plot $(\alpha h\nu)^2$ vs. hν. C) Tafel plot curves of the hematite microrobots under dark and light irradiation in pure water. D) Average speed at various concentrations of $H_2O_2$ under UV-light irradiation. Trajectories of hematite microrobots in E) 0.05% $H_2O_2$ and F) 1% $H_2O_2$, scale bars are 10 μm. G) The motility mechanism of hematite microrobots in a

high concentration of $H_2O_2$. Yellow arrows represent the motion direction of microrobots.

Hematite microparticles are intrinsically magnetic, as previously demonstrated.[37] The magnetic hysteresis loop of hematite microspheres was measured using a vibrating sample magnetometer (VSM) and plotted in **Figure 3A**, suggesting a ferromagnetic behavior. Hematite microrobots can perform a rolling motion along their long axis when applying a rotating magnetic field, and move in the perpendicular direction, as depicted in **Figure 3B**. Time-lapse images in **Figure 3C**, captured from **Supplementary Movie 2** and **Supplementary Movie 3**, illustrate that under a rotating magnetic field of 3 and 5 mT at different frequencies, varying from 5Hz to 30 Hz, a hematite microrobot rotated along its long axis and moved toward the orthogonal direction. The propulsion trajectories of hematite microrobots exhibited a significant decline in a predefined time as the magnetic field frequency was more significant. **Figure 3D** shows that the speed of microrobots linearly increases with the frequency up to a maximum velocity of 22 $\mu m\ s^{-1}$ under a rotating magnetic field of 5 mT at 10 Hz, known as the "step-out" frequency. Above this frequency, the speed significantly decreases, which is ascribed to the circumstance that the magnetic torque is not sufficient to maintain a synchronous relationship between the magnetic moment and the rotating magnetic field.[38, 39] This behavior agrees with the previously reported peanut motors that are transversely magnetized and is consistent with the trajectories shown in **Figure 3C**.[38] In addition, **Figure 3E** shows that the hematite microrobot swims along a predefined "nano" track in a rolling mode (**Supplementary Movie 4**), which indicates that hematite microrobots can be precisely controlled and navigated to specific locations, holding tremendous potential for biological applications.

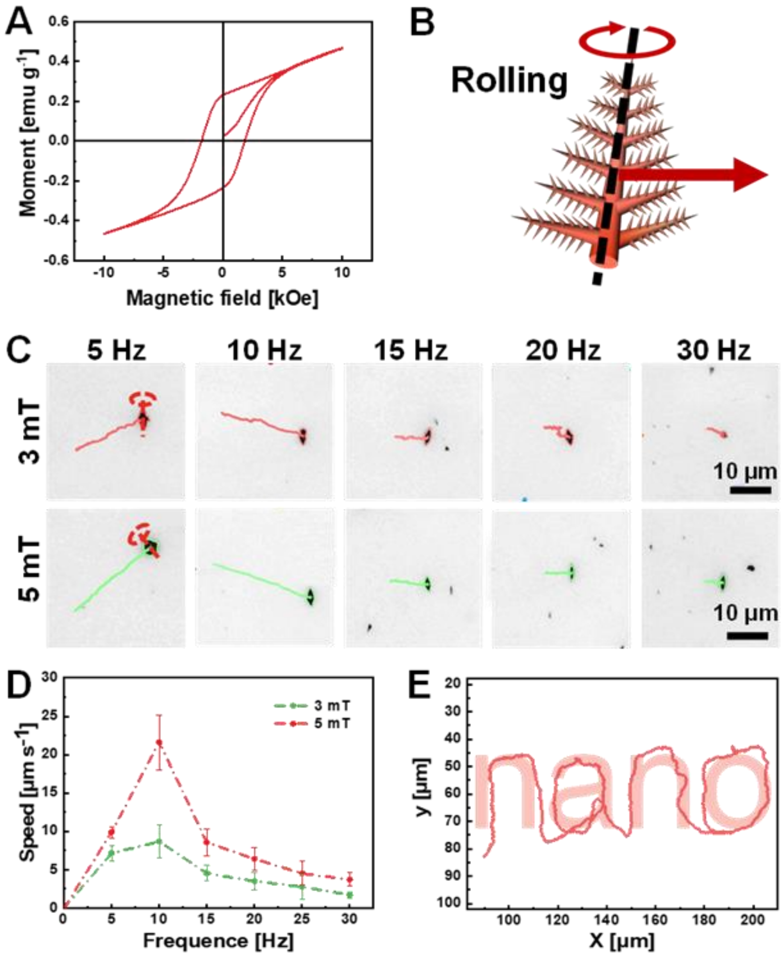

**Figure 3**. Magnetic actuation of hematite microrobots. A) Magnetic hysteresis loops of hematite microparticles. B) The scheme of a hematite microrobot in a rolling mode under a rotating magnetic field. C) Representative tracking trajectories of hematite microrobots under a rotating magnetic field of 3 mT and 5 mT at different frequencies for 5 s. Dashed lines represent the long axis of hematite microrobots and the sense of revolution. D) Corresponding speeds of microrobots under a rotating magnetic field. E) Trajectory of a hematite microrobot following a predesigned "nano" track.

Controllable and precise cell transportation is of significant interest concerning on-demand therapy, such as targeted cell/drug delivery and single-cell study.[40] There are two types of methods for cell manipulation: contact and non-contact. To achieve a more flexible actuation in a defined space, the non-contact manipulation of microrobots holds great advantages in non-contamination and remote control for biological applications. The locomotion of hematite microrobots can be flexibly controlled by adjusting the external rotating magnetic field parameters. Moreover, the rotation of the peculiar fin-like structure pumps the surrounding fluid to generate a localized hydrodynamic flow field capable of manipulating targeted cells without contact.[41] Yeast cells were selected as a cell model. As shown in **Figure 4A**, captured from **Supplementary Movie 5**, the yeast cell is synchronously moved along with the microrobots, exhibiting a linear trajectory. Considering the complex bio-microenvironments, we also control the locomotion of microrobots to transport the cell in a circle trajectory (**Figure 4B**), demonstrating that hematite microrobots can realize controllable non-contact cell transportation in arbitrary trajectories. **Figure 4C** displays the synchronized locomotion trajectories of the microrobot and the yeast cells under magnetic field navigation. By carefully manipulating the movement of the single microrobot along a predesigned trajectory, the target yeast cell was successfully driven along a similar path, showing an average transportation speed of ~2.8 μm $s^{-1}$ (**Figure 4D**). Furthermore, it is highlighted that there is no overlap between these two trajectories, which further indicates that hematite microrobots can realize the non-contact transportation of targeted objects along desired paths, enabling a significant benefit for future biomedical applications.

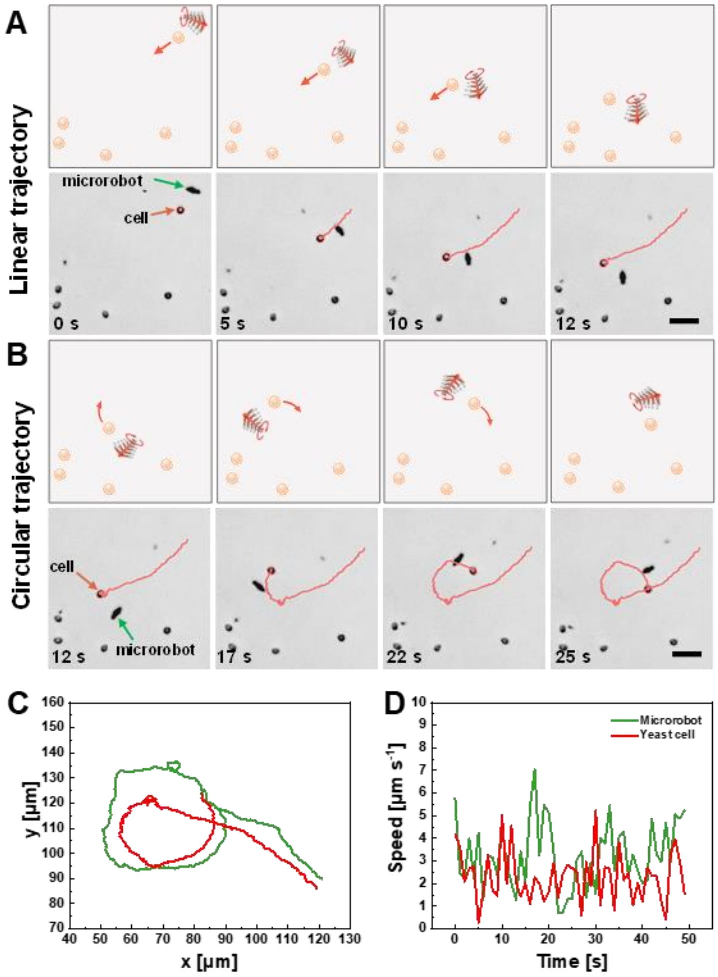

**Figure 4**. Controllable non-contact cell transportation. A) Linear transport of yeast cells and B) circular transport of yeast cells under a rotating magnetic field of 5 mT at 10 Hz. Red curves show the trajectory of the targeted cell. Red arrows beside the cell show the transport direction. Scale bars are 20 μm. C) Trajectories of the microrobot and transported yeast cell. D) Speed of the microrobot and transported yeast cell along the circular path.

Drug-free therapeutics, defined as a therapeutic methodology in which no drugs are involved, based on photocatalytic materials is highly desirable.[27] The ROS produced by the photocatalyst can oxidize GSH into oxidized glutathione (GSSG) to destroy the antioxidant microenvironment and increase the cytotoxicity against cancer cells. The effect of hematite microrobots in eliminating GSH was examined using 5,5′-dithiobis (2-nitrobenzoic acid) (DTNB) as an indicator since it reacts with GSH to form a yellow 5-thio-2-nitrobenzoic acid anion which can be monitored by UV-Vis spectroscopy.[42] As shown in **Figure S1A**, DTNB has an absorption peak of 323 nm. After the addition of GSH, the peak at 323 nm disappeared. Instead, a new peak at 408 nm appeared, indicating the formation of the 5-thio-2-nitrobenzoic acid anion. Initially, we investigated GSH consumption using hematite microrobots under different conditions: 1) microrobots + GSH; 2) microrobots + GSH + blue light; 3) microrobots + GSH + magnetic stirring; 4) microrobots + GSH + fuel (0.05% $H_2O_2$); 5) microrobots + GSH + fuel (0.05% $H_2O_2$) + blue light (**Figure S1**). As shown in **Figure 5A**, GSH content significantly decreased to 22% after the treatment with hematite microrobots under light illumination in $H_2O_2$ fuel. The microrobots can consume a relatively high amount of GSH thanks to the photo-Fenton reaction that enhances ROS production to oxidize GSH in the solution. **Figure 5B** displays the variation of GSH concentration over time. After 60 min treatment, microrobots can consume 8 mM GSH. In order to investigate the main ROS responsible for GSH consumption, radical trapping experiments were carried out, as shown in **Figure 5C**. In this regard, EDTA (10 mg $L^{-1}$), isopropanol (0.25 μL $mL^{-1}$), and nitro-blue tetrazolium (NBT, 10 mg $L^{-1}$) were chosen as trapping agents to capture photogenerated holes, •OH, and $•O^{2-}$, respectively.[43] The addition of both isopropanol and NBT dramatically increases the photocatalytic efficiency of the microrobots, resulting in 14% and 12%, respectively. On the contrary, the addition of EDTA decreased the GSH consumption, indicating that the scavenging of holes by EDTA inhibits the GSH oxidation. On this basis, it was concluded that the photogenerated holes are the main active species responsible for GSH depletion and may boost the microrobots' cytotoxicity for cancer cell treatment (**Figure 5D**).

Since hematite microrobots can increase ROS production and oxidize GSH, they were applied for "proof of concept" in vitro PDT therapy of prostate cancer cells. The cytotoxicity of hematite microrobots was investigated first. From **Figure 5F**, the hematite microrobots have no effect on the viability of prostate cancer cells in the absence of fuel ($H_2O_2$) and light irradiation. After 9 h incubation, no apparent cytotoxicity was noted at a microrobots' concentration of 1 mg $mL^{-1}$ (**Figure S3**), suggesting the high biocompatibility of hematite microcatalysts. The effect of fuel (0.05% $H_2O_2$) and light irradiation (485 nm, 48 mW $cm^{-2}$) on the viability of prostate cancer cells were also conducted to exclude other potential contributions, demonstrating just a mild decrease (88%), whereas, in the simultaneous presence of hematite microrobots, the cell viability significantly decreases down to 24% (**Figure 5F and**

**Figure S2**). To visualize cell killing efficiency, Calcein AM and propidium iodide (PI) co-staining experiments were conducted to validate the obtained results. Calcein AM can stain live cells in green fluorescence, while PI can stain dead cells in red fluorescence. The cell viability and morphology of the prostate cancer cells were observed under the fluorescent microscope, as shown in **Figure 5F**. Almost no cells in the control group were stained in red, indicating that only a few cells were killed. In the microrobots-free treated group (fuel + light) and microrobots + light treated group, a few cells were stained in red, indicating a weak PDT effect. In contrast, the number of dead cells observed in treatments involving microrobots + fuel + light was significantly increased, demonstrating once again that the microrobots show enhanced cytotoxicity by the photo-Fenton reaction to kill the majority of cancer cells.

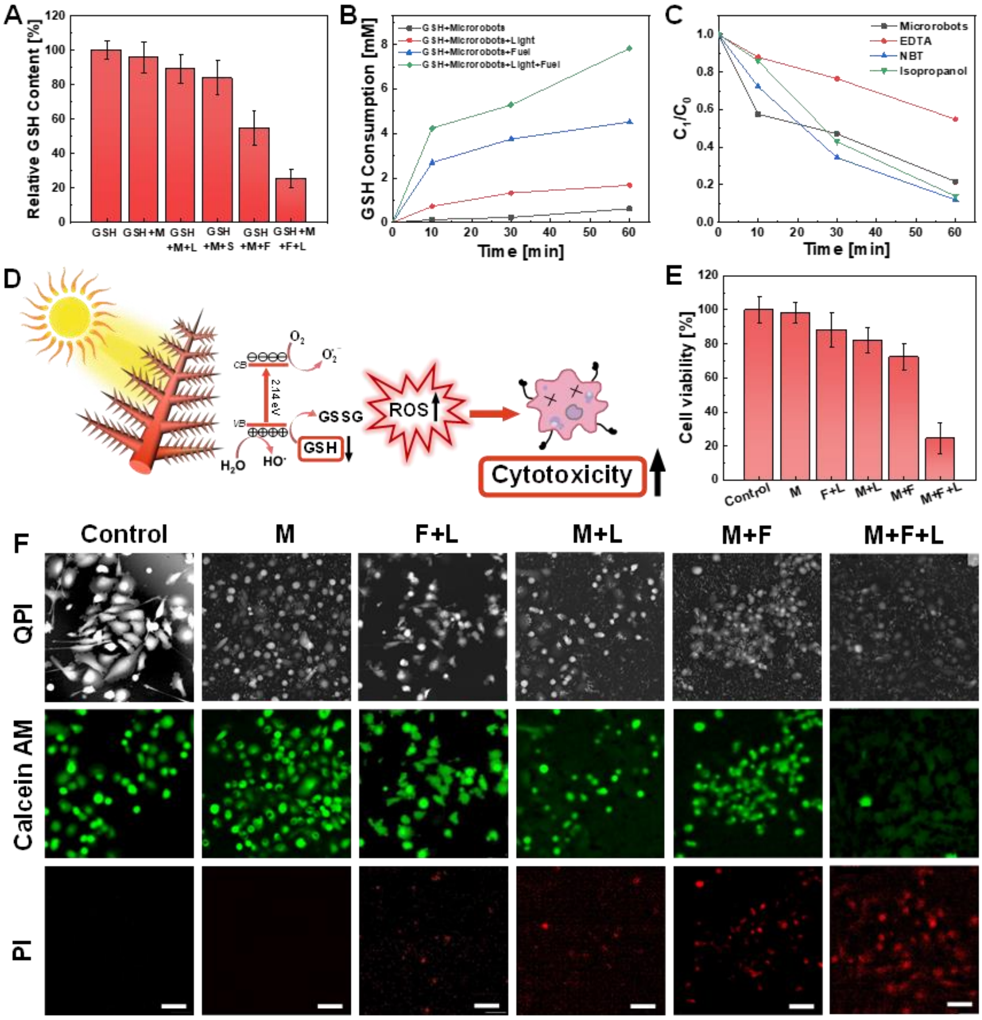

**Figure 5.** A) GSH consumption under different conditions (GSH + M: GSH + Microrobots; GSH + M + L: GSH + Microrobots + Light; GSH + M + S： GSH + Microrobots + Stirring; GSH + M + F： GSH

+ Microrobots + Fuel; GSH + M + F + L: GSH + Microrobots + Fuel + Light.) B) GSH consumption as a function of time. C) Radical trapping experiments performed using hematite microrobots with and without the presence of EDTA, NBT, and isopropanol; D) The proposed mechanism and scheme for therapy performances based on hematite microrobots. E) Cell viability after treatment at different conditions (F + L: Fuel + Light; M: Microrobots; M + L: Microrobots + Light; M + F: Microrobots + Fuel; M + F + L: Microrobots + Fuel + Light). F) Calcein AM (live cells) and PI (dead cells) staining method to investigate the death of prostate cancer cells induced by different conditions. Scale bars are 50 μm.

## Conclusion

In summary, we developed fin-shaped photocatalytic magnetic hematite microrobots by a low-cost and one-step hydrothermal method to realize the on-site generation of ROS to trigger prostate cancer cells therapy by GSH depletion. These microrobots exhibited dual light /magnetic-driven propulsion without integrating multiple components, undergoing negative photogravitaxis under light irradiation from the bottom and controllable actuation along a predefined path under the action of an external rotating magnetic field. Non-contact transportation of micro-objects, such as cells, was demonstrated by manipulating the movement of a single microrobot, which produced a powerful fluid flow pushing the targeted cell. Moreover, the hematite microrobots presented good biocompatibility. In vitro experiments proved that hematite microrobots can induce GSH oxidation upon reaction with the ROS generated by the photo-Fenton reaction, enhancing the PDT efficacy toward prostate cancer cells. Overall, the proposed drug-free PDT by fin-shaped hematite microrobots holds excellent potential for future clinical applications.

## Experimental section

**Preparation of hematite microrobots**: Typically, 0.1975 g of $K_3[Fe(CN)_6]$ (Sigma Aldrich, 99%) and 0.45 g of PEG-4000 (Mw: 4000, Alfa Aesar) were dissolved in 30 mL of DI water (18 MΩ cm) under vigorous stirring for 30 min to form a homogeneous yellow solution. The as-prepared solution was transferred into a 50 mL Teflon-lined stainless autoclave. Then, the autoclave was sealed and kept at 160 °C for 6 h. After the solution was cooled to room temperature naturally, the precipitate was collected by centrifugation (4000 rpm for 5 min) and washed with DI water and ethanol several times. Finally, the obtained product was dried in the oven at 60 °C overnight.

**Characterization of hematite microrobots:** The morphology and elemental analysis of the microrobots was characterized by scanning electron microscopy (SEM, MIRA3-XMU) equipped with an energy-dispersive X-ray (EDX) detector (Oxford Instruments). The crystal structure was measured by X-ray diffraction (XRD, Rigaku SmartLab 3 kW diffractometer, Cu Kα radiation). The chemical states were determined by X-ray photoelectron spectroscopy (XPS) using an Axis Supra spectrometer (Kratos Analytical), and the spectra were analyzed and fitted using CASA XPS software. All peaks were calibrated to the adventitious C 1*s* peak at 284.8 eV.

**Electrochemical measurements:** Tafel experiments were conducted using a customized photoelectrochemical setup with a 365 nm UV LED (700 mA powered LZ4-04UV00, LedEngin Inc.). An Ag/AgCl electrode was used as both the reference and counter electrode. The hematite working electrode was made by dropping 100 μL of a 5 mg $mL^{-1}$ aqueous suspension of hematite microrobots on an ITO-covered glass slide (1 x 2 $cm^2$, Sigma Aldrich, 8–12 Ω $sq^{-1}$ surface resistivity), and overnight drying. Tafel measurements were recorded at a scan rate of 5 mV $s^{-1}$ from -0.1 to 0.6 V vs. Ag/AgCl with/without UV-light irradiation on the working electrode in pure water using a Metrohm AUTOLAB potentiostat.

**Motion analysis of hematite microrobots:** The videos of microrobots' motion were captured at 25 fps by an inverted optical microscope (Nikon ECLIPSE TS2R) coupled with different microscope objectives (4x, 10x, and 40x), a Basler digital camera acA1920-155uc, and Pylon Viewer software. An external UV-LED (365 nm, pE-100) with a light intensity of 1.674 W $cm^{-2}$ coupled to the optical microscope was used. Microrobots' speed was evaluated in different concentrations (0, 0.5, 1, 2, 3%) of $H_2O_2$ (Sigma Aldrich, 30%). Magnetic field-controlled navigation experiments were performed using a homemade magnetic controller system consisting of three orthogonal coil pairs in a 3D-printed polylactic acid (PLA) backbone, which generated a transversal rotating magnetic field. Navigation experiments were performed with an applied magnetic field of 3mT and 5mT at different frequencies from 5 to 30 Hz. The recorded videos were analyzed by NIS Elements Advanced Research software.

**Detection of GSH consumption in vitro**: GSH concentration was quantitatively determined using the Ellmann probe (5,5′-dithiobis-(2-nitrobenzoic acid), DTNB). The fresh aqueous solutions of DTNB (Sigma Aldrich, 2.5 mg $mL^{-1}$) and GSH (Sigma Aldrich, 10 mM) were prepared. 1 mg hematite microrobots and 20 μL GSH were added into 980 μL phosphate buffer solution (PBS, pH=7.4) and irradiated with a solar simulator for different periods (10–60 min). The microrobots in the solution were removed by centrifugation (4000 rpm for 3 min), and 990 μL supernatant and 10 μL DTNB solution were added to a transparent cuvette for further UV-Vis absorption measurements. The decrease of the absorbance at 412 nm was measured to calculate the concentration and then the consumption of GSH based on **Equation (2)**:

$$Consumption\ (\%) = \frac{C_0 - C_t}{C_0} \times 100, \tag{2}$$

where $C_0$ is the initial GSH concentration and $C_t$ is the GSH concentration after the treatment with microrobots at different reaction times, measured in correspondence with the maximum of 412 nm in the UV-Vis spectra.

**In vitro cytotoxicity assessment:** Human PC-3 prostate cancer cells were used in this work. The PC-3 cell line was established from grade 4 prostatic adenocarcinoma from 62 years old Caucasian male and derived from the metastatic site in bones. The PC-3 cell line was purchased from HPA Culture Collections (Salisbury, UK). PC-3 cells were cultured in Ham's F12 medium with 7% PBS. The medium was supplemented with penicillin/streptomycin (100 U/ml), and the cells were maintained at 37°C in a humidified incubator with 5% $CO_2$.

QPI imaging was performed using a multimodal holographic microscope Q-PHASE (Telight a.s., Brno, CZ). The cells were cultivated in Flow chambers μ-Slide I Lauer Family (Ibidi, Martinsried, Germany). To maintain standard cultivation conditions (37 °C, humidified air (60%) with 5% $CO_2$) during time-lapse experiments, the cells were placed in the gas chamber H201 - for Mad City Labs Z100/Z500 piezo Z-stages (Okolab, Ottaviano NA, Italy). To image enough cells in one field of view, Nikon Plan 10/0.30 was chosen. For all selected experimental conditions, seven fields of view were observed with a frame rate of 3 min frame$^{-1}$ for 24h, respectively. Holograms were captured by a CCD camera (XIMEA MR4021 MC-VELETA), and fluorescence images were captured using ANDOR Zyla 5.5 sCMOS camera. Complete quantitative phase image reconstruction and image processing were performed in Q-PHASE control software. Cell dry mass values were derived according to [44] and [45] according to **Equation (3)**

$$m = \frac{\varphi\lambda}{2\pi\alpha} \tag{3}$$

where $m$ is cell dry mass density (in pg μm$^{-2}$), $\varphi$ is detected phase (in rad), $\lambda$ is wavelength in μm (0.65 μm in Q-PHASE), and $\alpha$ is specific refraction increment (≈0.18 μm$^{3}$ pg$^{-1}$). All values in the formula except the $\varphi$ are constant. The value of $\varphi$ is measured directly by the microscope. Integrated phase shift through a cell is proportional to its dry mass, which enables studying changes in cell mass distribution.[45] Cell dry mass tracking was performed using the Q-PHASE SophIQ software (Telight a.s., Brno, CZ).

For the hematite microrobots' excitation, samples were irradiated with a 485 nm light with a 25 nm bandwidth. A light dose of 24 mJ cm$^{-2}$ was achieved by the combination of time exposition (500 ms) and light intensity (48 mW cm$^{-2}$). Viability during quantitative phase imaging was evaluated using Calcein AM, which allows visualization of live cells, and PI, which labels dead cells after the loss of cell membrane integrity (Merck, Germany). A module attached to a Q-PHASE microscope with FITC (Calcein AM) and TRITC (PI) filters were used for fluorescence imaging.

## Acknowledgments

This work was supported by the Ministry of Health of the Czech Republic (NU21-08-00407). M.U. acknowledges the financial support by the European Union's Horizon 2020 research and innovation program under the Marie Skłodowska-Curie grant agreement No. 101038066.

## Reference

[1] Ibele, M.; Mallouk, T. E.; Sen, A. Schooling Behavior of Light-Powered Autonomous Micromotors in Water. *Angew. Chem. Int. Ed.* **2009**, *121*, 3358–3362.

[2] Dong, R.; Zhang, Q.; Gao, W.; Pei, A.; Ren, B. Highly Efficient Light-Driven $TiO_2$-Au Janus Micromotors. *ACS Nano* **2016**, *10*, 839–844.

[3] Palagi, S.; Singh, D. P.; Fischer, P. Light-Controlled Micromotors and Soft Microrobots. *Adv. Opt. Mater.* **2019**, *7*, 1–18.

[4] Fernández-Medina, M.; Ramos-Docampo, M. A.; Hovorka, O.; Salgueiriño, V.; Städler, B. Recent Advances in Nano- and Micromotors. *Adv. Funct. Mater.* **2020**, *30*, 1908283.

[5] Zhou, M.; Xing, Y.; Li, X.; Du, X.; Xu, T.; Zhang, X. Cancer Cell Membrane Camouflaged Semi-Yolk@Spiky-Shell Nanomotor for Enhanced Cell Adhesion and Synergistic Therapy. *Small* **2020**, *16*, 1–11.

[6] Darmawan, B. A.; Gong, D.; Park, H. G.; Jeong, S.; Go, G.; Kim, S. J.; Zheng, S.; Nan, M.; Nguyen, V. D.; Bang, D.; Kim, C.; Kim, H.; Park, J.; Choi, E. Magnetically Controlled Reversible Shape-morphing Microrobots with Real-time X-ray Imaging for Stomach Cancer Applications. *J. Mater. Chem. B* **2022**, *10*, 4509–4518.

[7] Jurado-Sánchez, B.; Wang, J. Micromotors for Environmental Applications: A Review. *Environ. Sci. Nano* **2018**, *5*, 1530–1544.

[8] Urso M.; Pumera, M. Nano/Microplastics Capture and Degradation by Autonomous Nano/Microrobots: A Perspective. *Adv. Funct. Mater.* **2022**, *32*, 2112120.

[9] Peng, X.; Urso, M.; Ussia, M.; Pumera, M. Shape-Controlled Self-Assembly of Light-Powered Microrobots into Ordered Microchains for Cells Transport and Water Remediation. *ACS Nano* **2021**, *16*, 7615-7625.

[10] Hong, Y.; Diaz, M.; Córdova-Fteueroa, U. M.; Sen, A. Light-Driven Titanium-Dioxide-Based Reversible Microfireworks and Micromotor/Micropump Systems. *Adv. Funct. Mater.* **2010**, *20*, 1568–1576.

[11] Ussia, M.; Urso, M.; Kment, S.; Fialova, T.; Klima, K.; Dolezelikova, K.; Pumera, M. Light-Propelled Nanorobots for Facial Titanium Implants Biofilms Removal. *Small* **2022**, *18,* 1–10.

[12] Dong, R.; Hu, Y.; Wu, Y.; Gao, W.; Ren, B.; Wang, Q.; Cai, Y. Visible-Light-Driven BiOI-Based Janus Micromotor in Pure Water. *J. Am. Chem. Soc.* **2017**, *139*, 1722–1725.

[13] Oral, C. M.; Ussia, M.; Yavuz, D. K.; Pumera, M. Shape Engineering of $TiO_2$ Microrobots for ‘On-the-Fly’ Optical Brake. *Small* **2022**, *18*, 1–6.

[14] Zhang, Q.; Dong, R.; Wu, Y.; Gao, W.; He, Z.; Ren, B. Light-Driven Au-$WO_3$@C Janus Micromotors for Rapid Photodegradation of Dye Pollutants. *ACS Appl. Mater. Inter.* **2017**, *9*, 4674–4683.

[15] Vizsnyiczai, G.; Frangipane, G.; Maggi, C.; Saglimbeni, F.; Bianchi, S.; Di Leonardo, R. Light Controlled 3D Micromotors Powered by Bacteria. *Nat. Commun.* **2017**, *8*, 1–7.

[16] He, X.; Jiang, H.; Li, J.; Ma, Y.; Fu, B.; Hu, C. Dipole-Moment Induced Phototaxis and Fuel-Free Propulsion of ZnO/Pt Janus Micromotors. *Small* **2021**, *17*, 1–11.

[17] Lyu, X.; Liu, X.; Zhou, C.; Duan, S.; Xu, P.; Dai, J.; Chen, X.; Peng, Y.; Cui, D.; Tang, J.; Ma, X.; Wang, W. Active, Yet Little Mobility: Asymmetric Decomposition of $H_2O_2$ Is Not Sufficient in Propelling Catalytic Micromotors. *J. Am. Chem. Soc.* **2021**, *143*, 12154–12164.

[18] Urso, M.; Iffelsberger, C.; Mayorga-Martinez, C. C.; Pumera, M. Nickel Sulfide Microrockets as Self-Propelled Energy Storage Devices to Power Electronic Circuits ‘On-Demand. *Small Methods* 2021*, 2100511,* 1–9.

[19] Pacheco, M.; Jurado-Sánchez, B.; Escarpa, A. Visible-Light-Driven Janus Microvehicles in Biological Media. *Angew. Chem. Int. Ed* **2019**, *58*, 18017–18024.

[20] Chen, W.; Zhou, H.; Zhang, B.; Cao, Q.; Wang, B.; Ma, X. Recent Progress of Micro/Nanorobots for Cell Delivery and Manipulation. *Adv. Funct. Mater.* **2022**, *32*, 2110625.

[21] Xie, Z.; Fan, T.; An, J.; Choi, W.; Duo, Y.; Ge, Y.; Zhang, B.; Nie, G.; Xie, N.; Zheng, T.; Chen, Y.; Zhang, H.; Kim, J. S. Emerging Combination Strategies with Phototherapy in Cancer Nanomedicine. *Chem. Soc. Rev.* **2020**, *49*, 8065–8087.

[22] Wu, W.; Mao, D.; Hu, F.; Xu, S.; Chen, C.; Zhang, C.; Cheng, X.; Yuan, Y.; Ding, D.; Kong, D.; Liu, B. A Highly Efficient and Photostable Photosensitizer with Near-Infrared Aggregation-Induced Emission for Image-Guided Photodynamic Anticancer Therapy. *Adv. Mater.* **2017**, *29*, 1700548.

[23] W. Piao et al., Development of An Azo-Based Photosensitizer Activated under Mild Hypoxia for Photodynamic Therapy. *J. Am. Chem. Soc.* **2017**, *139*, 13713-13719.

[24] Piao, W.; Hanaoka, K.; Fujisawa, T.; Takeuchi, S.; Komatsu, T.; Ueno, T.; Terai, T.; Tahara, T.; Nagano, T.; Urano, Y. An Amphiphilic Ruthenium Polymetallodrug for Combined Photodynamic Therapy and Photochemotherapy. In Vivo. *Adv. Mater.* **2017**, *29*, 1603702.

[25] Ma, Y.; Li, X.; Li, A.; Yang, P.; Zhang, C.; Tang, B. $H_2S$-Activable MOF Nanoparticle Photosensitizer for Effective Photodynamic Therapy against Cancer with Controllable Singlet-Oxygen Release. *Angew. Chem. Int. Ed.* **2017**, *56*, 13752–13756.

[26] Zhou, Z.; Song, J.; Nie, L.; Chen, X. Reactive Oxygen Species Generating Systems Meeting Challenges of Photodynamic Cancer Therapy. *Chem. Soc. Rev.* **2016**, *45*, 6597–6626.

[27] Zhao, B.; Wang, Y.; Yao, X.; Chen, D.; Fan, M.; Jin, Z.; He, Q. Photocatalysis-Mediated Drug-Free Sustainable Cancer Therapy Using Nanocatalyst. *Nat. Commun.* **2021**, *12*, 1–11.

[28] Urso, M.; Ussia, M.; Pumera, M. Breaking Polymer Chains with Self-Propelled Light-Controlled Navigable Hematite Microrobots. *Adv. Funct. Mater.* **2021**, *2101510*, 1–10.

[29] Bagus, P. S.; Nelin, C. J.; Brundle, C. R.; Lahiri, N.; Ilton, E. S.; Rosso, K. M.; Analysis of the Fe 2*p* XPS for Hematite α-$Fe_2O_3$: Consequences of Covalent Bonding and Orbital Splittings on Multiplet Splittings. *J. Chem. Phys.***2020**, *152*, 014704.

[30] Villa, K.; Novotný, F.; Zelenka, J.; Browne, M. P.; Ruml, T.; Pumera, M. Visible-Light-Driven Single-Component $BiVO_4$ Micromotors with the Autonomous Ability for Capturing Microorganisms. *ACS Nano* **2019**, *13*, 8135–8145.

[31] Villa, K.; Děkanovský, L.; Plutnar, J.; Kosina, J.; Pumera, M. Swarming of Perovskite-Like $Bi_2WO_6$ Microrobots Destroy Textile Fibers under Visible Light. *Adv. Funct. Mater.* **2020**, *30*, 2007073.

[32] Feng, Y.; Lin, S.; Huang, S.; Shrestha, S.; Conibeer, G. Can Tauc Plot Extrapolation Be Used for Direct-Band-Gap Semiconductor Nanocrystals? *J. Appl. Phys.* **2015**, *117*, 125701.

[33] Zhou, D.; Ren, L.; Li, Y.; Xu, P.; Gao, Y.; Zhang, G.; Wang, W.; Mallouk, T. E.; Li, L. Visible Light-Driven, Magnetically Steerable Gold/Iron Oxide Nanomotors. *Chem. Commun.* **2017**, *53*, 11465–11468.

[34] Singh, D. P.; Uspal, W. E.; Popescu, M. N.; Wilson, L. G.; Fischer, P. Photogravitactic Microswimmers. *Adv. Funct. Mater.* **2018**, *28*, 1706660.

[35] Zhang, J.; Mou, F.; Tang, S.; Kauffman, J. E.; Sen, A.; Guan, J. Photochemical Micromotor of Eccentric Core in Isotropic Hollow Shell Exhibiting Multimodal Motion Behavior. *Appl. Mater. Today* **2022**, *26*, 101371.

[36] Urso, M.; Ussia, M.; Novotný, F.; Pumera, M. Trapping and Detecting Nanoplastics by MXene-Derived Oxide Microrobots. *Nat. Commun.***2022**, *91*, 1–14.

[37] Peng, X.; Urso, M.; Pumera, M. Photo-Fenton Degradation of Nitroaromatic Explosives by Light-Powered Hematite Microrobots: When Higher Speed Is Not What We Go For. *Small Methods* **2021**, *2100617*, 1–9.

[38] Lin, Z.; Fan, X.; Sun, M.; Gao, C.; He, Q.; Xie, H. Magnetically Actuated Peanut Colloid Motors for Cell Manipulation and Patterning. *ACS Nano* **2018**, *12*, 2539–2545.

[39] Muñoz, J.; Urso, M. Pumera, M. Self-Propelled Multifunctional Microrobots Harboring Chiral Supramolecular Selectors for 'Enantiorecognition-on-the-Fly,'" *Angew. Chem. Int. Ed.* **2022**, *61*, 1–7.

[40] Chen, Y.; Chen, D.; Liang, S.; Dai, Y.; Bai, X.; Song, B.; Zhang, D.; Chen, H.; Feng, L. Recent Advances in Field-Controlled Micro–Nano Manipulations and Micro–Nano Robots. *Adv. Intell. Syst.***2022**, *4*, 2100116.

[41] Pan, T.; Shi, Y.; Zhao, N.; Xiong, J.; Xiao, Y.; Xin, H.; Li, B. Bio-Micromotor Tweezers for Noninvasive Bio-Cargo Delivery and Precise Therapy. *Adv. Funct. Mater.* **2022**, *32*, 2111038.

[42] Muñoz, A.; Petering, D. H.; Shaw, F. C. Reactions of Electrophilic Reagents that Target the Thiolate Groups of Metallothionein Clusters: Preferential Reaction of the α-Domain with 5,5′-Dithio-Bis(2-Nitrobenzoate) (DTNB) and Aurothiomalate (AuSTm). *Inorg. Chem.* **1999**, *38*, 5655–5659.

[43] Jeong, M. S.; Yu, K.; Chung, H. H.; Park, S. J.; Lee, A. Y.; Song, M. R.; Cho, M.; Kim, J. S. Methodological Considerations of Electron Spin Resonance Spin Trapping Techniques for Measuring Reactive Oxygen Species Generated from Metal Oxide Nanomaterials. *Sci. Rep.* **2016**, *6*, 1–10.

[44] Prescher, J. A.; Bertozzi, C. R. Chemistry in Living Systems. *Nat. Chem. Biol.* **2005**, *1*, 13–21.

[45] Park, Y.; Depeursinge, C.; Popescu, G. Quantitative Phase Imaging in Biomedicine. *Nat.*

*Photon.* **2018**, *12*, 578–589.